Elevated temperature, nano-mechanical testing *in situ* in the scanning electron microscope

J. M. Wheeler[a] and J. Michler
EMPA – Swiss Federal Laboratories for Materials Science and Technology, Laboratory for Mechanics of Materials and Nanostructures, Feuerwerkerstrasse 39, Thun CH-3602, Switzerland

(Received 26 September 2012; accepted 5 March 2013; published online 3 April 2013)

A general nano-mechanical test platform capable of performing variable temperature and variable strain rate testing *in situ* in the scanning electron microscope is described. A variety of test geometries are possible in combination with focused ion beam machining or other fabrication techniques: indentation, micro-compression, cantilever bending, and scratch testing. The system is intrinsically displacement-controlled, which allows it to function directly as a micro-scale thermomechanical test frame. Stable, elevated temperature indentation/micro-compression requires the indenter tip and the sample to be in thermal equilibrium to prevent thermal displacement drift due to thermal expansion. This is achieved through independent heating and temperature monitoring of both the indenter tip and sample. Furthermore, the apex temperature of the indenter tip is calibrated, which allows it to act as a referenced surface temperature probe during contact. A full description of the system is provided, and the effects of indenter geometry and of radiation on imaging conditions are discussed. The stabilization time and temperature distribution throughout the system as a function of temperature is characterized. The advantages of temperature monitoring and thermal calibration of the indenter tip are illustrated, which include the possibility of local thermal conductivity measurement. Finally, validation results using nanoindentation on fused silica and micro-compression of ⟨100⟩ silicon micro-pillars as a function of temperature up to 500 °C are presented, and procedures and considerations taken for these measurements are discussed. A brittle to ductile transition from fracture to splitting then plastic deformation is directly observed in the SEM for silicon as a function of temperature. [http://dx.doi.org/10.1063/1.4795829]

I. INTRODUCTION

Nano-mechanical testing *in situ* inside the scanning electron microscope (SEM) has become increasingly popular due to the scaling down of sample dimensions below the lateral resolution of optical methods. Small scale samples such as MEMS devices, thin films, individual microstructural phases within alloys, and other small features of interest require micro-nano scale mechanical test methods, and *in situ* testing in the SEM is ideal for these applications. This is partly due to positioning requirements, but real time visualization during deformation is also a highly attractive analytical tool. The advantages of *in situ* testing in the SEM and the various systems available have been detailed in several recent reviews.[1–3]

Development of *in situ* systems has typically focused on increasing force/displacement resolution, generating different loading cases or incorporating additional analytical techniques such as scanning topography,[4,5] EBSD,[6,7] Raman,[8] or electrical measurements.[9–11] Very few *in situ* systems[12] have been developed for varying the environmental conditions, such as temperature. *Ex situ* systems, most notably nanoindentation systems, have been developed in this direction considerably more.[13–15] Several commercial[15,16] and custom-modified[14,17,18] systems have now been adapted for high temperature usage with varying degrees of thermal stability achieved within different temperature ranges.

The determining factor for the thermal stability at elevated temperatures of these systems appears to be the amount of thermal control allowed by the system. A very high degree of thermal control and stability is required for nano-scale mechanical testing, since temperature variations in any of several different system components of even small fractions of a degree Celsius can produce tens of nanometers of thermal expansion. Thermal gradients may be present in the system, but they must be stable and remain fixed during contact and testing. If heat flows between various system components, this produces accompanying thermal expansions which manifest as thermal drift.

In systems where only the sample is heated, thermal drift and noise have been observed to increase with the temperature[14,16] due to the increasing thermal gradient proportionally increasing the amount of heat flow. Additional thermal control measures such as water cooling, insulating the indenter tip, and passively heating the indenter by leaving the tip in contact for a stabilization period can reduce the temperature gradient between the tip and the sample and the flow of heat into sensitive components. These techniques can reduce the thermal drift, however thermal drift is still observed to increase with increasing temperature. Independently heating and monitoring the temperature of both the indenter and the sample adds the ultimate degree of thermal control. Smith and Zheng[19] first demonstrated this technology for instrumented

[a]E-mail: Jeffrey.Wheeler@empa.ch

indentation, and further work from indentation systems in this series has consistently demonstrated low thermal drift (<0.1 nm/s) at high temperature.[15,18,20–29] Using this technique, stable operation in vacuum at high temperatures has also been demonstrated.[17,18,29–31]

Once stable, low thermal drift operation is attained at a target temperature, then the accuracy of the determination of the true temperature at the contact must be addressed. For passively heated indenters, large thermal gradients on the order of 10% would be expected at the contact, as will be shown in later sections. With actively heated indenters, the indenter and sample temperature can be matched using displacement drift tuning techniques.[15] However, thermal gradient between the contacting surfaces and the control thermocouples within the heaters results in temperature uncertainty. For large, thermally homogenous samples, this can be addressed by attaching a third thermocouple to the sample surface,[29] but a more general solution can be achieved by calibrating the thermal gradient between the indenter tip and the indenter heater's control thermocouple.[32]

By combining *in situ* testing in the SEM with elevated temperature techniques,[17] a unique and powerful capability for observing and measuring thermally activated deformation mechanisms can be achieved. Slip systems for plastic deformation can be directly observed[30] without secondary imaging. Video of various transitions such as phase transformations,[33] glass transitions,[31] deformation twinning, or various chemical reactions can all be directly observed and recorded. Fracture behavior, crack lengths, and ductile-brittle transformations can all also be observed. Synergistically, *in situ* operation in the SEM provides a high vacuum (10^{-6} mBar) environment for imaging, which also removes the danger of diamond indenter oxidation at temperatures >400 °C.[34] Also, in addition to the imaging capabilities necessary for positioning and deformation observation, the SEM also automatically provides the vibration damping necessary for nano-scale measurements.

In this work, we describe a general nano-mechanical testing system capable of variable temperature testing *in situ* in the SEM, which combines the benefits of elevated temperature testing with *in situ* observation and positioning. The work is structured as follows. The design of the system is described first; followed by examining the effects of temperature on the system. Next, the various factors related to the effects of temperature differences at the contacting surfaces and methods for resolving these issues are presented. Finally, the procedures for and results from materials property measurements using nanoindentation and micro-compression on reference materials are discussed.

II. INSTRUMENTATION

In this section, the specific design aspects and capabilities of the system and the effects of indenter geometry and heating on *in situ* imaging will be discussed. This provides a first background on the system's intrinsic capabilities before the more specific issues of heating are discussed with relation to this system in later sections.

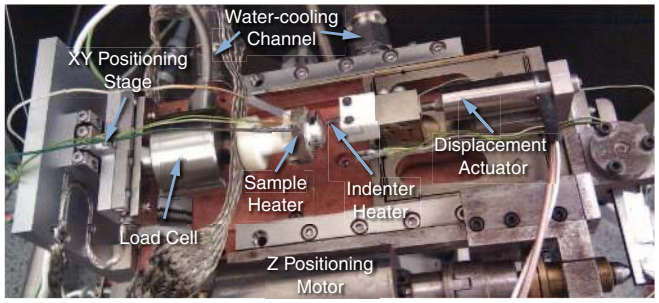

FIG. 1. Alemnis *In Situ* Indenter with modifications for elevated temperature operation.

A. System description

The elevated temperature, *in situ* nano-mechanical testing system consists of a Zeiss DSM 962 SEM with an Alemnis *In Situ* Indenter, first developed by Rabe *et al.*[35] and more recently described by Ghisleni *et al.*[36] This base system has been extensively modified here for operation at elevated temperature by incorporating tip and sample heating on independent thermocouple proportional-integral-derivative (PID) controlled feedback loops with the option of constant heating power at desired temperatures (Figure 1). The major frame components of the system have been replaced with high thermal conductivity copper and aluminum alloy components, and water-cooling has been integrated into the copper baseplate. To protect the load cell from excessive heat, nickel-coated copper braid was used to provide a thermal short-circuit to a low thermal resistance escape path for heat from the sample heater.

Other system modifications, in addition to elevated temperature components, have also been made since the initial development of the system. Sample positioning stages have been upgraded from the original system design to nanometer precision SmarAct SLC-1740 actuators. System data acquisition and control electronics have been upgraded to current 24-bit National Instruments cDAQ modules managed with custom LabView software. The displacement piezoelectric actuator has a range of 20 μm with a noise floor standard deviation of 0.3 nm, and the load cell has a maximum force of 500 mN with a noise floor standard deviation of 6 μN. Water-cooling has been observed to have no significant effect on the noise floor of either sensor.

The system is intrinsically displacement-controlled. The piezoelectric actuator, which is compensated for piezoelectric relaxation with a strain gauge for feedback, imposes a set displacement to the sample which then transmits the load to the load cell behind it. Thus, in simple loading cases, such as tension or compression, constant or variable strain rate testing is straightforward to achieve by simply varying the imposed displacement rate. To accurately achieve a specific desired strain rate, the frame compliance must be taken into account before choosing the appropriate displacement rate. As compliance is load dependent, the strength of the sample must be measured first, and then the appropriate correction can be made. Displacement control is particularly beneficial after plastic yielding has occurred, where stress rate approximations of

constant strain rates using load-controlled devices would cause a rapid increase in the strain rate due to yielding. Strain rate jump indentations and micro-compressions[30] have also been demonstrated using this system.

Using a PID feedback loop in the software control, this intrinsically displacement-controlled device can also be used in a pseudo load-controlled mode. This allows conventional nanoindentation loading profiles to be utilized with constant load hold periods at maximum load for creep and 5% or 10% of maximum load for thermal drift. However, the system remains intrinsically displacement-controlled, so sudden yield events which would result in displacement bursts or pop-ins in a load-controlled system instead manifest as load drops.[17]

B. Effects on imaging conditions

A primary concern to any microscopist when utilizing an *in situ* testing system is: "How will this system affect the microscope?" Several issues have been dealt with during the development of this machine: heater power regulation, grounding of all wiring, and the effect of indenter geometry on imaging. First, typical commercial heater PID controller components operate on alternating current. This presents a problem, since an oscillating current inside the SEM will produce an oscillating deflection in the path of the electron beam or a wobbly image. This was remedied using a custom LabView software temperature controller which remotely controls a direct current power supply to the heaters. This also enables simple temperature logging capability, the utility of which will be discussed extensively later.

Next, all electrical components within the system must be thoroughly grounded. This prevents any exterior wires from acting as antennae and transmitting noise into the microscope.

Finally, the effect of the indenter geometry and viewing angle on imaging must be considered. In principle, *in situ* indentation can be performed using any indenter geometry. However, higher aspect ratio indenters, such as the Cube Corner geometry—Figure 2(a), provide a wider open angle for viewing. This has two benefits. First, the depth of field necessary to image the indentation is reduced due to higher observation angles, which allows sharper focus on the features of interest such as pile up, shear offsets, and cracks. Second, the wider open angle allows for significantly more secondary electrons to escape from the region of interest to be detected by the sensor. Low aspect ratio indenters, such as the Vickers or Berkovich geometry, effectively trap secondary electrons in the narrow open angle between the indenter and the sample. This is illustrated by the heavy shadowing underneath the Berkovich indenter in Figure 2(b). Due to the narrow angle of observation possible with a Berkovich indenter and the heavy shadowing, *in situ* testing with this type of indenter typically yields little observational or positioning benefits for large flat samples. Thus, a Cube Corner geometry is typically preferred for all *in situ* indentation measurements.

A final consideration for imaging at high temperatures is the effect of radiation. Above the Draper point at 525 °C,[37] nearly all solids begin to radiate in the infrared and visible spectrum. This results in a decrease in heating efficiency and increased distribution of heat throughout the chamber. Many materials also begin thermionic emission of electrons above this temperature with intensity depending on the work function of the material. This can result in a significant decrease in image contrast at elevated temperatures, since typical secondary electron detectors cannot distinguish between thermally emitted electrons and secondary electrons from the scanning electron beam.

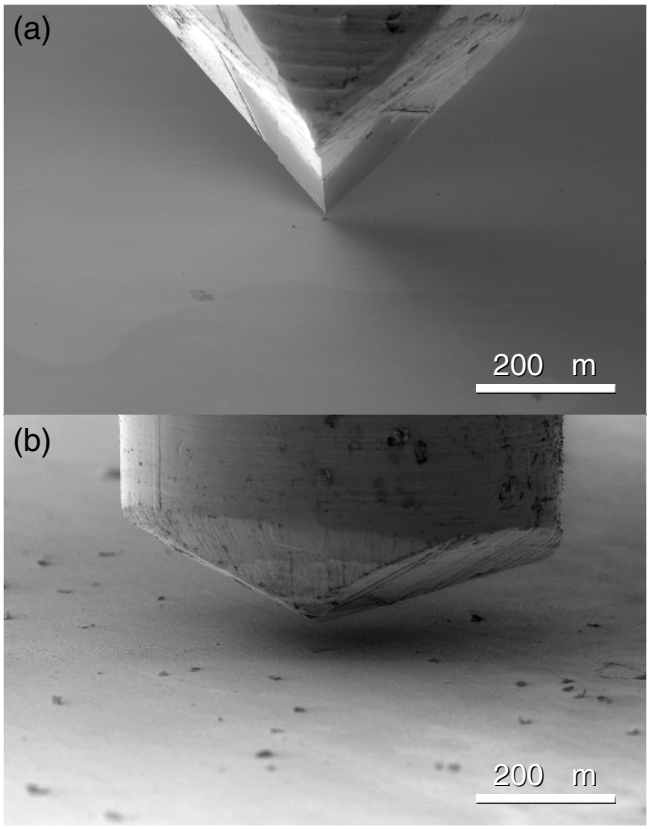

FIG. 2. Secondary electron imaging using (a) a Cube Corner indenter at an observation angle of 21.2° and (b) a Berkovich indenter at an observation angle of 10.6°.

III. SYSTEM CHARACTERIZATION

Before any testing can begin, it is important to know what changes, if any, occur to the system's performance and sensor/actuator calibrations. In this section, the stabilization of the system as a function of time for imposed temperature changes of varying magnitude and direction are examined, and then the temperature distribution within the system at various temperatures is investigated. This provides confidence that the sensors/actuators are still within their calibrated range of temperatures for operation. Knowledge of what expected values of thermal drift due to stabilization of temperature gradients within the frame as a function of time enables a user to determine whether the observed drift is due to stabilization or due to a temperature mismatch at the contact during testing.

A. System stabilization time

In order to perform any fine scale mechanical test, a stable system is required to minimize the effect of any environmental changes, such as ambient fluctuations in air currents or temperature, during the test on the results. This is especially true on the nano-scale where displacements and forces to be measured are on the same order or below that of environmental fluctuations.

To describe thermal drift, a distinction must first be made between the normal thermal stabilization period of a system at ambient temperature and the stabilization of a system at elevated temperatures. In the first case, the temperature gradients are very small and scattered throughout the indentation system's frame as well as between the indenter and sample. This kind of drift is normally managed in most systems by placing the indentation system inside a thermally managed cabinet with a built-in thermostat or a series of cabinets or baffles to thermally lag the system, which prevents any thermal variation being introduced into the system. Any thermal variation introduced by opening the cabinet, inserting a new sample or changing the system temperature is gradually stabilized through conduction and, in atmosphere, convection. In ambient conditions, a high level of thermal stability can typically be achieved over a period of hours. This type of drift, which can be removed by a stabilization period, can be designated as *system thermal drift*. This is the displacement drift which is measured by a hold period prior to indentation. At ambient temperatures, this drift rate is generally similar to the drift measured during a hold after unloading.

For this system, the thermal variations introduced are due mainly to either the change in pressure during pumping to vacuum, which results in cooling of small thermal mass components due to the ideal gas law, or to imposed changes to the sample and/or indenter heaters: i.e., stabilization at elevated temperatures. Since both the load cell and the displacement piezoelectric actuator contain sensors, the drift in both signals can be directly measured as a function of time during stabilization from such an event (Figure 3).

Vacuum pumping is seen to introduce a sharp variation in the load drift and smaller variations in temperature or displacement drift. This is attributed to the internal components inside the load cell being affected by the pressure change-induced temperature drop as the interior of the load cell is evacuated.

Sensor drifts during stabilization at elevated temperatures are observed to scale in both magnitude and stabilization time with the scale of the temperature change imposed. Despite relatively rapid heating rates on the order of 100 °C/min and the apparently stable temperature values at elevated temperature, the system is observed to take approximately ten times longer to stabilize than to achieve the maximum temperature. However, this time period, which includes heating, is still on the order of minutes rather than the hours previously reported using larger systems without cooling.[18] This highlights the advantage of using a compact system composed of high thermal conductivity frame components with active cooling.

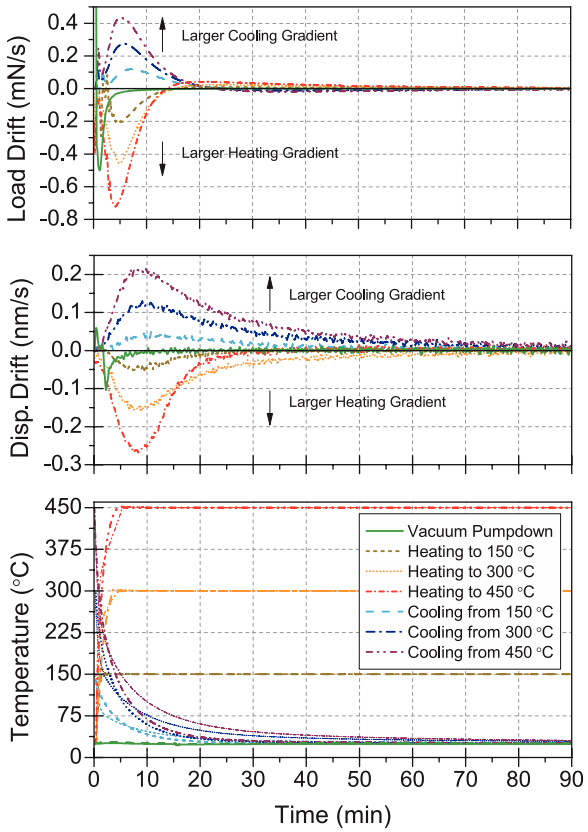

FIG. 3. Load and displacement sensor drift during and after heating and cooling to various temperatures with the indenter temperature shown with smaller line thickness.

B. System temperature

In order to achieve accurate results within the calibrated temperature range of the load and displacement sensors, the high temperature region of the system or hot zone must be kept localized to the region of interest. This is achieved via a combination of insulating components, high thermal conductivity escape paths for heat and water-cooling of the overall system. The effectiveness of these solutions is shown in Figure 4, which schematically illustrates the projected temperature distribution based on thermocouple measurements shown in Figure 4(b) at the locations denoted by the green and yellow dashed lines in Figures 4(a) and 4(c). This is achieved using small, efficient heaters contained in insulating components in high vacuum. This prevents heat flow via convection from circumventing the insulations. The efficiency of this is highlighted by the thermal gradient between a surface-mounted thermocouple and the indenter thermocouple midway down the indenter shaft. The gradients between the indenter thermocouple and the sample surface and their utility are further discussed in Sec. IV.

IV. INDENTER THERMAL MONITORING AND CONTROL

With the system stable at the desired temperature, the conditions at the contact are the next concern for a user. In this section, the complications due to temperature mismatches

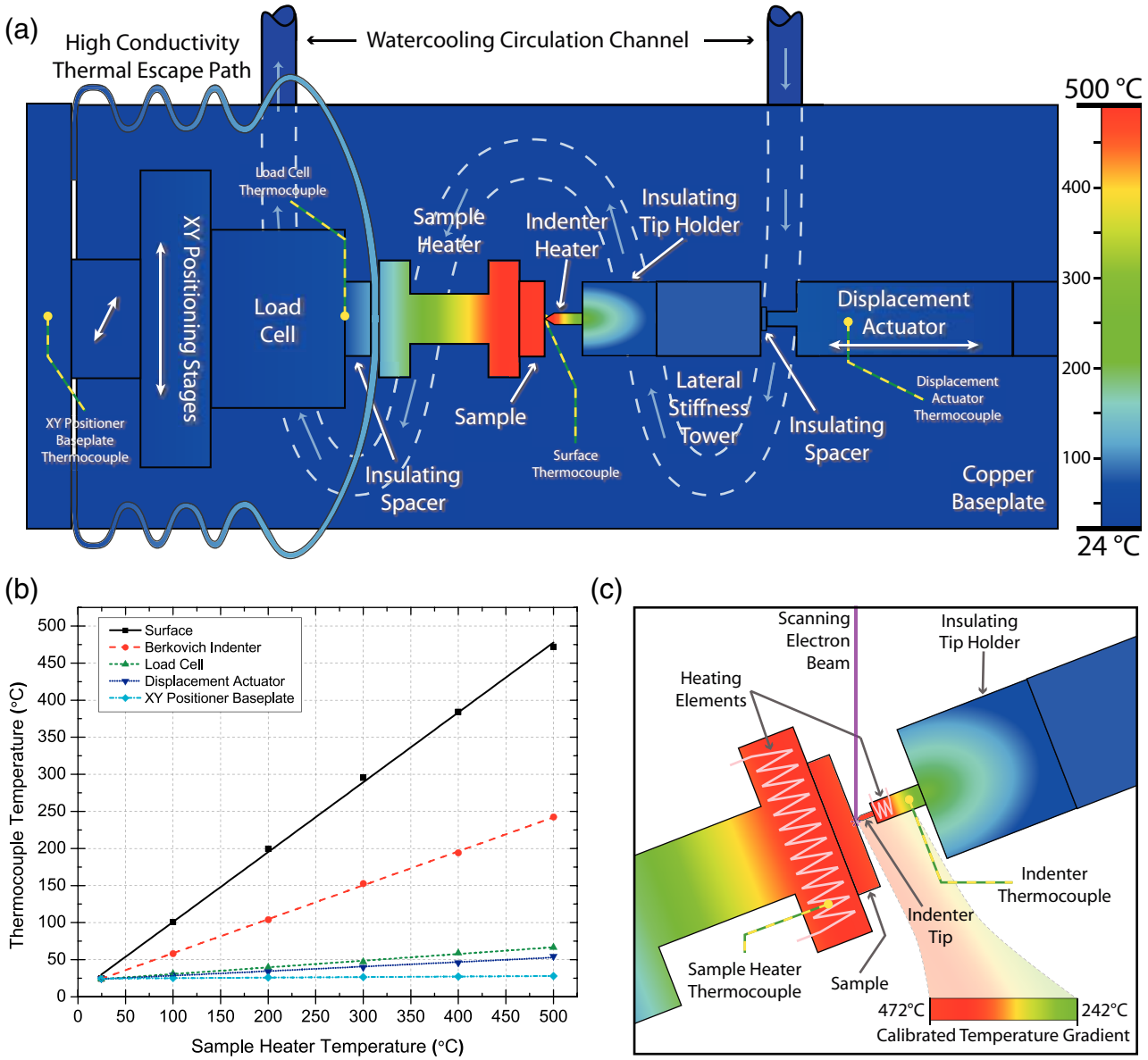

FIG. 4. Temperature within the nanomechanical testing system with (a) a top view schematic diagram of the temperature in the system with the sample heater at 500 °C and the indenter apex temperature matched with the surface temperature with the locations of thermocouples denoted by yellow and green dashed lines, (b) the measured temperature gradient from the thermocouples as a function of the sample heater temperature, and (c) a close-up side view of the temperatures near the contact as oriented in the SEM at an observation angle of 21.2°.

between the indenter and the sample and solutions for addressing this are presented. First, the effects of a mismatch in temperature between the sample and the indenter on the temperatures at the contact are illustrated by thermometry. Second, the effects of this mismatch on load-displacement data are described along with the relationship between temperature variations during contact and displacement. These relationships are then exploited as an alternative method of temperature matching. Next, the effect of different methods of temperature regulation (PID vs. constant heating power) on measured temperatures and displacements is discussed. Following this, the new method of temperature matching using temperature shift measurements during contact is used to calibrate the temperature gradient between the indenter's control thermocouple and the indenter tip. Lastly, the sensitivity of the thermal measurements possible using this method are examined for materials of different thermal conductivity.

A. Effect of temperature mismatch on sample temperature and thermal drift

By monitoring the temperatures at the contact, the thermal situation can be quickly determined. The small scale of the sample/indenter contact makes this challenging, but existing technology can still yield several insights. Figure 5(a) shows the variation in temperature during a Cube Corner indentation into a 0.5 mm diameter thermocouple junction. The sample heater was set to a nominal temperature of 100 °C, while the indenter was only passively heated to 37 °C prior to contact via the limited convection possible at 10^{-5} mBar.

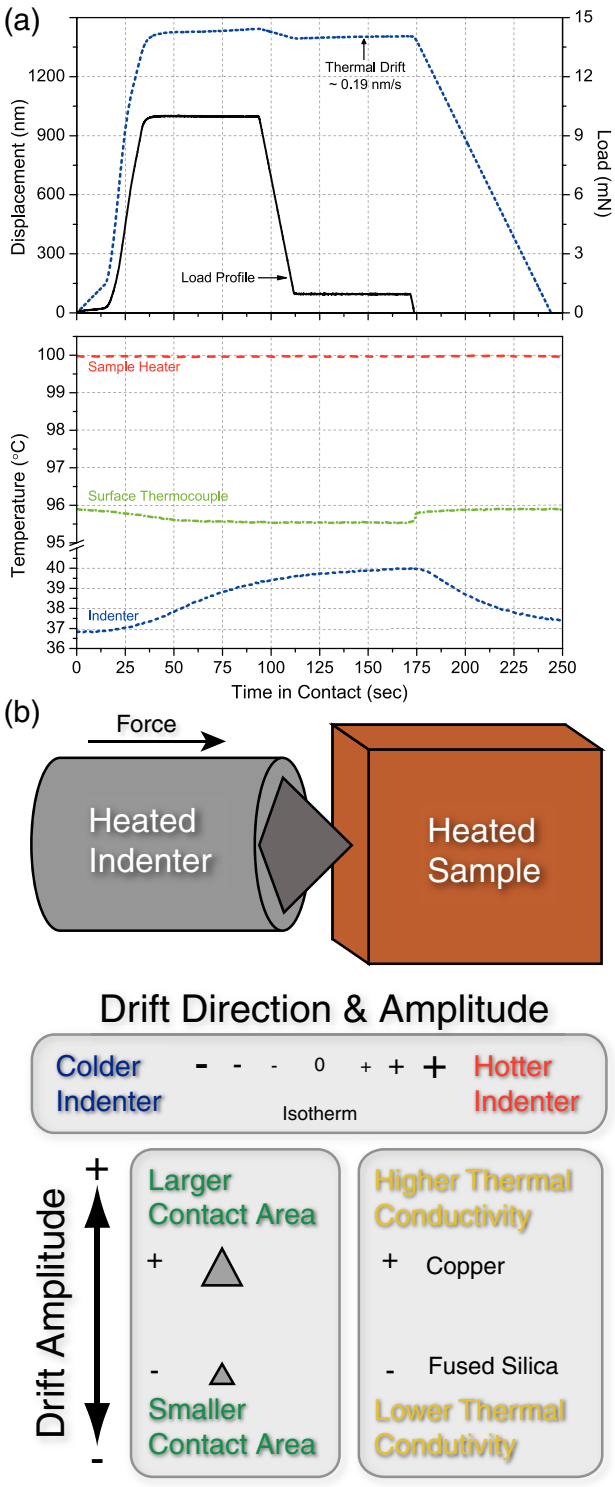

FIG. 5. The effects of temperature mismatch on (a) indenter and surface/sample temperature during contact and (b) general effects of contact variables on thermal drift.

During contact, the "cold" indenter is observed to receive heat from the hotter sample and increase in temperature by 3 °C, which is 5% of the temperature difference between the indenter thermocouple and the surface thermocouple. However, it is known[32] that the magnitude of the thermal gradient between the indenter thermocouple and the indenter tip is significant (further discussed in Sec. IV D), so the actual change in temperature at the tip is thought to be much larger than measured temperature shift during contact. The actual temperature variations at the contact may be an order of magnitude larger, ~30 °C, which would correspond to half of the temperature difference between the sample and indenter prior to contact. Despite this projected magnification of the measured temperature, the temperature of the indenter is observed to rapidly approach a stable asymptote at values significantly below the sample temperature. It is unlikely that the indenter could be passively heated to the same temperature as the sample with a hold period of any length.

It is also significant to note that the temperature of the thermocouple being indented changes during contact, in addition to the indenter. The measured drop is only 0.5 °C, however, this implies that the temperature of a significant fraction of the ~65 × 10^6 μm^3 volume of the thermocouple junction dropped 0.5 °C due to an indentation with a total plastic volume on the order of 100 μm^3 – 4 orders of magnitude smaller! This strongly suggests that the local temperature of the indentation plastic zone is being significantly affected by the temperature mismatch between indenter and sample. This provides some experimental confirmation of the finite element model predictions from Everitt *et al.*,[15] which showed thermal gradients between 25%–50% occurring in the plastic zone for indentation using a passively heated indenter.

These temperature changes during contact between samples and indenters of different temperatures also result in thermal expansions. These thermal expansions manifest in displacement measurements as thermal displacement drift. This type of drift can be designated as *contact thermal drift*, as it only manifests during contact between the indenter and sample. Without precise contact surface temperature calibrations, temperature mismatches between indenter and sample will only increase with increasing temperature, and drift will persist despite a stabilization period of any length. The magnitude and direction of this drift depends on the direction and magnitude of the heat flow occurring, and the general effects of different contact variables on this can be projected as shown in Figure 5(b).

Expansions can also occur within the system frame due to heat flow from a temperature change, such as changing sample/indenter temperature as discussed earlier, causing thermal expansions inside the system yielding *frame drift*. This type of drift stabilizes as the thermal gradients establish into a stable pattern similar to sensor stabilization shown previously in Figure 3.

B. Displacement variation due to temperature mismatch

When both the indenter and sample are heated and thermal gradients are stabilized, thermal displacement drift is a function of the degree of precision to which the surface temperatures of the sample and indenter are matched. Related work on other systems[15,28,38] has suggested temperature matching procedures where the thermal displacement drift is measured for several different indenter temperatures above or below the sample temperature—similar to the measurements shown in Figure 6(a). When an indenter temperature is found

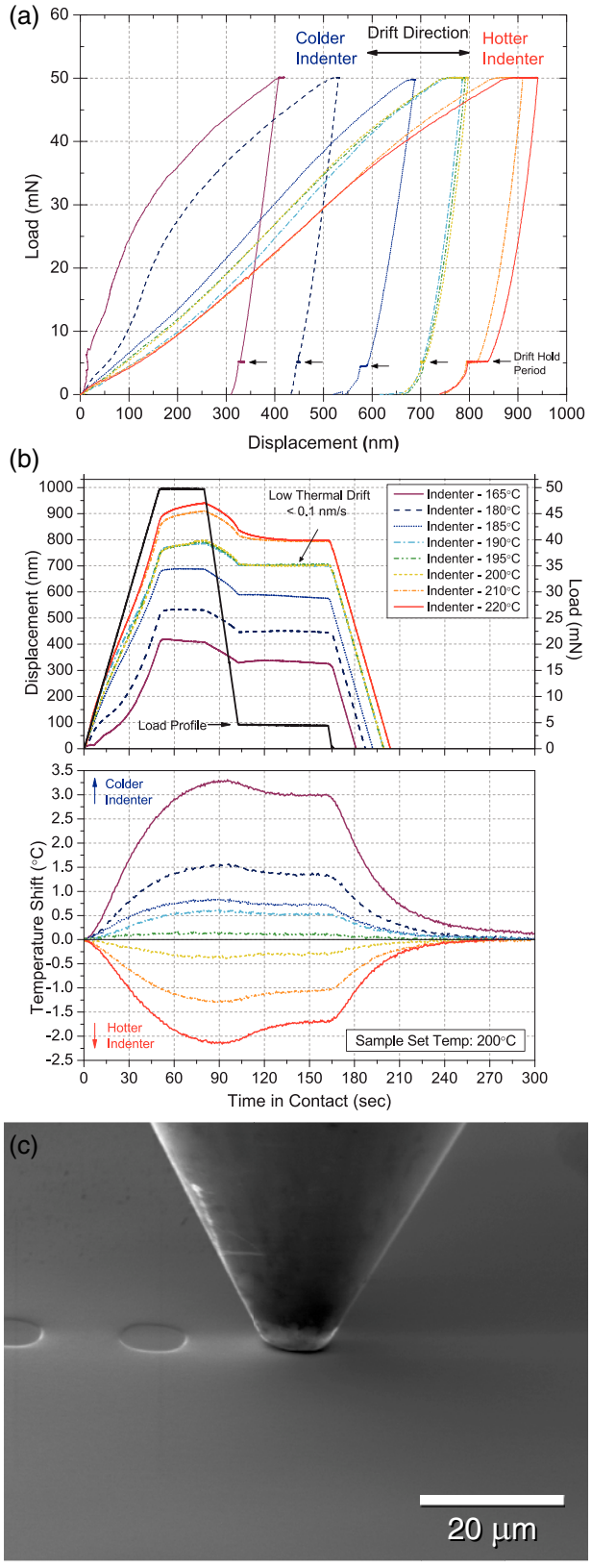

FIG. 6. Load-displacement curves (a) obtained in pseudo load-controlled indentations on a tantalum sample heated to a nominal temperature of 200 °C using a thermally calibrated, 9 μm diameter diamond flat punch with the indenter at various temperatures, (b) displacement and indenter temperature measurements as a function of time, and (c) *in situ* SE micrograph of the contact.

where the displacement drift reaches a minimum, the temperatures are assumed to be aligned at an isotherm. However, this assumes that thermal displacement drift is solely dependent on temperature difference prior to contact. Instead, the measured displacement drift is the sum of the *frame drift* and the *contact drift*. Thus, it is not a direct method for identifying if the temperatures between the indenter and surface are matched, since they could be matched while still measuring displacement due to *frame drift*.

Instead, using temperature measurements, rather than displacement measurements, of the indenter temperature under constant heating power during contact is suggested. By this method, described previously,[32] the variation in indenter temperature is used as an indicator of the temperature difference between the sample and indenter. Profiles of indenter temperature shift as a function of contact time can be generated by using the same loading profile to achieve similar contact areas, varying the indenter temperature prior to contact and holding the heater power to the indenter at a constant level during indentation. The overall amplitude of these profiles is observed to directly depend on the thermal gradient between the indenter and the sample, and the temperature shift is also shown to be dependent on the displacement into the sample. An example of this type of temperature tuning is shown in Figure 6(b).

Figure 6 shows the effects of *contact drift* on load-controlled, flat punch indentations on tantalum at 200 °C. The effects of thermal drift on displacement-controlled testing are discussed elsewhere.[30–32] In general, if the indenter tip is colder than the sample, the indenter acquires heat and begins to expand upon contact. In load control, this gives the appearance of the indenter withdrawing from the sample or negative displacement drift, at constant load. This is the case observed by systems operating without indenter tip heating.[14] If the indenter is hotter than the sample, it yields heat to the sample and contracts, which gives the opposite appearance: positive displacement drift. This can be seen in the overall shift of the curves in Figure 6(a).

When the sample and indenter temperatures are closely matched, as occurred in Figure 5 when the indenter was set to values near 195 °C, thermal displacement drift is observed to be significantly reduced. Here the thermal drift during the latter portion of the drift hold periods was ~0.06 nm/s at a sample temperature of 200 °C, which is an order of magnitude reduction from the drift levels observed in vacuum at the same temperature by Trenkle *et al.*[14] using a Macor® indenter holder shaft similar to that used here without indenter heating. Low levels of drift at temperatures higher than 500 °C have also been reported in inert atmosphere[15] and in vacuum[18] using indenter and sample heating. Thermal drift levels which are independent of sample/indenter temperature are demonstrated with this system in Sec. V of this work.

The variations in temperature observed in Figure 5(b) during contact offer an answer to why thermal drift may be nonlinear during some contact situations, especially for indenters where the contact area can change during unloading: conical, pyramidal and spherical indenters. Here, with a flat punch indenter, the temperature shift magnitude is observed to decrease upon unloading to the drift hold period. These

temperatures are observed still to be stabilizing to the new contact conditions during the initial portion of the drift hold period, which directly corresponds to the initial nonlinearity in the displacement-time relationship. When the indenter is set to 165 °C prior to contact, the temperature can still be observed to be decreasing at 120 s of contact time. This decreasing temperature corresponds to a thermal contraction of the indenter, resulting in the appearance of positive drift during the initial portion of the drift hold period. A similar, but opposite, trend is observed when the indenter temperature was set to 220 °C prior to contact. This variability in thermal displacement drift during contact highlights the necessity for close matching of the indenter and sample temperature prior to testing.

C. Effect of PID regulation on contact temperatures

Nearly all heater controllers utilize a form of PID control to reach and maintain a setpoint temperature or heating rate. In this system, a software controller is used, which allows easy variation of the different time constants used in the feedback control. Prior to contact, the PID control is used to quickly reach a desired setpoint temperature and stabilize the system at that value as shown previously in Figure 3.

During contact, however, if the indenter and sample are not matched in temperature, as discussed in Sec. IV B, the indenter temperature can vary during contact as a result of heat flow to/from the larger sample/sample heater. If the indenter temperature begins to change, its PID feedback controller will adjust the heating power to compensate. In Figure 7, this is shown for the case of the indenter being colder than the sample. This results in the indenter gaining heat from the sample, then the PID controller responds by reducing heating power. This causes the indenter to contract, reducing the apparent displacement. Figure 7(a) shows that this PID reaction increases the deviation of the measured load-displacement curve from the "correct" curve where the temperatures are closely matched. Figure 7(b) shows how the temperature changes from the PID control relate to the displacement as a function of time.

The strength of this response will be dependent on the time constants used in the PID controller as well as the thermal mass and heating power available in the system. For example, if the proportional constant was too large, in this case, it would have resulted in the heating power being cut altogether, which would completely retract the indenter. If the integral constant was larger, it would have responded much more slowly, so that the heating power might not significantly change during the indentation or effectively keep the power constant. Lastly, if the differential constant of the PID controller was larger, it would result in imposing a sinusoidal variation on the temperature. This would, in turn, impose a sinusoidal variation in indenter displacement. This has been observed previously using a hardware PID controller.

Maintaining the heating power at a constant level is the preferred case, as it allows the temperature difference between the indenter and sample to control the indentation response rather than the PID's characteristics. Constant heating power after stabilization is used in all other places in this work.

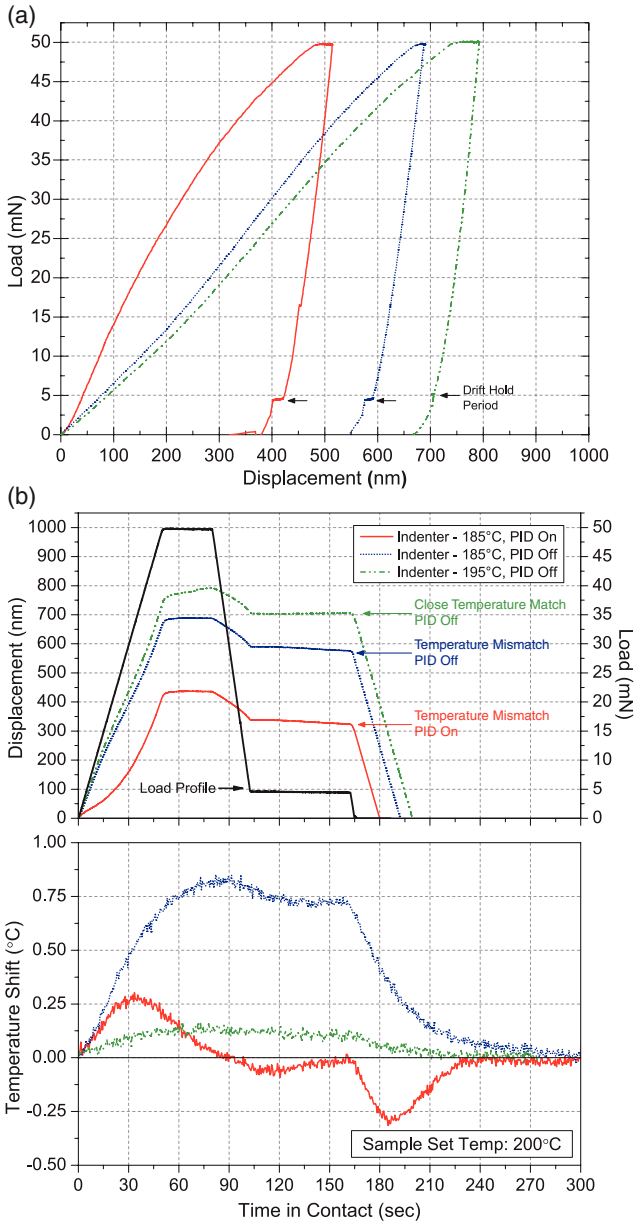

FIG. 7. Illustrative effect of PID regulation of the indenter temperature on (a) load-displacement curves and (b) the measured temperature and displacement with time.

D. Indenter thermal gradient calibration

Temperatures reported by the indenter/sample feedback thermocouples will not be the exact temperatures at the contact. This disparity between the nominal temperatures and the actual contact temperature is a function of the proximity of the feedback control thermocouples to the sample surface and the indenter tip as well as the thermal conductivities of the intervening material(s). On the sample side, this will vary as each sample's material, geometry and mounting will be unique. On the indenter side, the geometry and relation of the indenter tip to its control thermocouple will remain constant, enabling a calibration of the temperature gradient between the indenter tip and the indenter thermocouple.

By generating the temperature shift profiles shown in Sec. IV C, the indenter tip temperature can be precisely

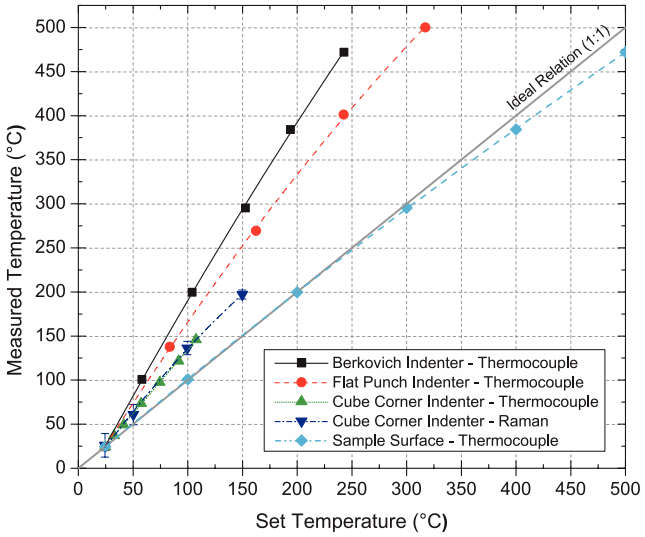

FIG. 8. Temperature calibration curves for the indenters used in this study and the cube corner indenter first calibrated by both thermocouple indentation and Raman spectroscopy.[32]

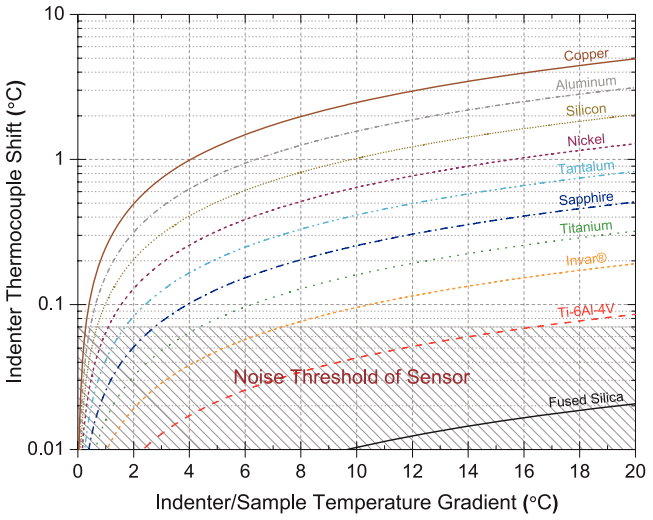

FIG. 9. Predicted indenter temperature shift upon contact as a function of the temperature difference between the indenter and sample surfaces.

matched to the contact surface temperature. By indenting a sample with a known surface temperature, such as a calibrated thermocouple junction, the indenter's true tip temperature can be determined as a function of its feedback thermocouple temperature. These relationships for the two indenters used in this work, and a third from a previous study,[32] are shown in Figure 8. Care must be taken in thermocouple type selection; Type K contains nickel and reacts with many indenter materials. Platinum-rhodium-based thermocouples (Types B, R, and S) are recommended for high temperature tip temperature calibration of diamond indenters. This method for thermally calibrating indenters is discussed in greater detail in previous work,[32] where indenter temperature calibrations were conducted by both Raman spectroscopy and thermocouple indentations. The error in these indenter thermal calibrations, and thus in accuracy of the surface temperature measurements using the indenter tip as a surface temperature probe, is typically $\sim$1% of the test temperature.

E. Indenter thermocouple sensitivity

By using a fine gauge (76 μm) thermocouple for the indenter tip feedback control, the response time of the thermocouple has been reduced to the order of a second, and, by using a 24-bit DAQ card, the temperature resolution of the thermocouples is $<$0.07 °C. This allows the temperature variation from contact to be observed directly during indentation. Previous measurements[32] have determined a specific heat or indenter sensitivity for this design of heated indenter to be a temperature shift of 0.1 °C/nW of heat flow.

Heat flow is the source of contact thermal drift. Thermal conductance obeys Fourier's law[39] for two dissimilar materials in contact:

$$q = \frac{T_{indenter} - T_{sample}}{\frac{\Delta x_{indenter}}{-k_{indenter} A} + \frac{1}{h_c A} + \frac{\Delta x_{sample}}{-k_{sample} A}}, \quad (1)$$

where Δx is the distance from the interface in meters, k is the thermal conductivity in W m^{-1} K^{-1}, A is the contact area in m^2, and h_c is the conductance coefficient, h_c. The thermal conductance coefficient term is neglected in this analysis with the assumption of a perfect, uniform new surface formed at extremely high pressure during the indentation. The contact surface area of the indenter was used instead of the projected cross-sectional area, since the projected cross section will only act as a bottleneck to heat flow when the ratio of surface area to projected area exceeds the ratio of thermal conductivities between the indenter and sample. This is unlikely to occur for diamond indenters ($k \approx 2000$ W m^{-1} K^{-1}) on most samples.

Using this relation and the known sensitivity of the instrument, the temperature shift during a 1 μm deep indentation with the calibrated cube corner indenter on a variety of sample materials of known thermal conductivity[40] can be predicted (Figure 9). This yields a linear relationship in temperature shift as a function of temperature gradient across the contact, but it is shown on a log scale to allow visualization of materials with over two orders of magnitude of variation in thermal conductivity. This illustrates the difficulty in matching sample and indenter temperatures on samples with low thermal conductivities, where thermal gradients of several degrees are required for the temperature shift to be detectable. However, on materials with even moderate thermal conductivity such as sapphire, temperature differences between sample and indenter of even a few degrees can be readily detected.

For materials with readily detectable temperature shifts during contact, by using a thermally calibrated indenter with a known sensitivity, the local thermal conductivity of the sample could also be measured. This would be accomplished by measuring the variation of the indenter temperature shift as a function of the indenter/sample temperature gradient as shown in Figure 9. Possible sources of error such as contact area variation could be minimized using a flat punch indenter, and pure metals such as copper and titanium could act as reference calibration standards. This would allow a novel

method for directly measuring the thermal conductivity of micro-objects such as nanowire or carbon nanotube brushes.

V. MATERIALS PROPERTY MEASUREMENTS

In this last section, the procedures for and results of measurements on reference materials using the previously described system and techniques are presented. First, the procedures for mounting a sample for elevated temperature, matching the indenter/sample temperature to a known value, and analysis of the resulting data are discussed. Next, in order to compare to other elevated temperature nanoindentation systems, results from Berkovich indentation of fused silica at elevated temperature are presented. Finally, results from micro-compression testing on silicon micro-pillars highlight the unique capability of this system to pair observation and measurement of transitions in deformation behavior with temperature.

A. Procedures and considerations

Mounting of samples for elevated temperature testing is not always straightforward. Most room temperature means of adhesively bonding samples for nanoindentation, e.g., cyanoacrylate or thermal wax, decompose at elevated temperature. A variety of cements are available which are suitable for elevated temperature usage, however they typically involve a drying period as well as an elevated temperature final cure. For samples which do not readily oxidize at elevated temperature in air, this is straightforward. The sample can be mounted, bonded, and cured at elevated temperature *in situ* on the sample heater. This can then be degassed in a separate vacuum chamber to avoid contamination to the microscope. However, if the sample oxidizes at desired temperature, either a second vacuum chamber complete with feedthroughs for heating is necessary to cure and degas the bonded arrangement or this may be done inside the microscope at the risk of some additional hydrocarbon contamination of the chamber.

For a typical elevated temperature indentation or micro-compression test, the indenter and sample heaters are set to heat to the desired setpoint temperature under PID control. After an initial stabilization period at the target temperature of approximately 10 min, prior to full system stabilization (Figure 3), the indenter can be switched to constant heating power to perform temperature tuning indentations to match the indenter and sample surface temperatures as shown in Figure 10. Since this temperature matching process is accomplished using temperature measurements instead of displacement drift measurements, the temperatures can be accurately matched while the thermal gradients within the system frame are still stabilizing. This is significantly more time efficient than displacement drift measurements, since displacement drift measurements would require the frame to be completely stable before a direct relationship between drift and indenter/sample temperature mismatch would be expected. A typical tuning procedure might involve indentations at 4 or 5 different indenter/sample temperatures and last approximately 1 h.

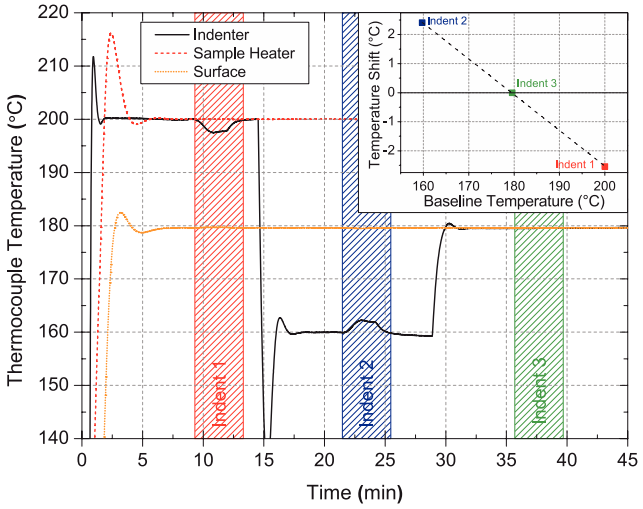

FIG. 10. An exemplar temperature matching procedure using indenter temperature shift magnitudes to infer the isothermal contact temperature, which coincides with surface thermocouple measurements.

Temperature tuning indentations can be performed with nearly any load profile, providing the profile is consistent amongst the test temperatures: it yields a nearly equivalent constant area. Pseudo load control, i.e., displacement control with a specified target load/loading rate on a software PID feedback loop, was performed using the loading profiles shown in Figure 6. A default displacement rate of 20 nm/s was used during displacement control approach and retraction. If the initial setpoint target for the indenter was correct, this temperature shift profile will measure no significant variation during contact. If the temperature is observed to change, the indenter setpoint temperature is adjusted in the opposite direction of the shift. This procedure is repeated until the indenter temperature is matched to the sample surface temperature. The inset of Figure 10 illustrates how the process can be expedited by plotting the trend of the maximum temperature shift against the indenter setpoint temperature and linearly extrapolating the shift to zero, where the temperatures match.

Elevated temperature property measurements were carried out on two reference materials by two methods: nanoindentations on fused silica and micro-compression of silicon micro-pillars. Indentations on fused silica were performed with a previously unused, other than for calibration indentations, Berkovich indenter using pseudo load control to a maximum load of 10 mN with a loading and unloading rate of 0.5 mN/s with dwell periods 30 s at maximum load and of 60 s at 1 mN. Micro-compressions of silicon were carried out using a constant strain rate of 10^{-3} s^{-1}. The appropriate displacement rates for this strain rate were determined from pillar height measurements taken *in situ* in the SEM prior to compression. Tuning indentations were performed prior to each set of measurements to ensure thermal drift would be at a minimum.

Indenter materials' properties, such as strength and Young's modulus, also change with increasing temperature. Using the correct modulus for the indenter material at the test temperature is important for accurate analysis. Figure 11 shows the variation of the Young's modulus of several major

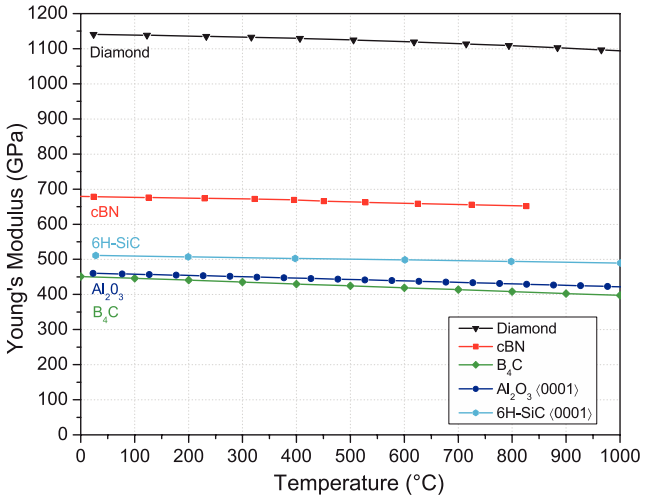

FIG. 11. Variation of Young's modulus with temperature of diamond,[41] cubic boron nitride,[41] boron carbide,[42] silicon carbide,[43] and sapphire.[44,45]

indenter materials with temperature. For diamond, cBN and SiC, this change is only a few percent over 500 °C. However, for B_4C and sapphire, the change over the same interval is ~6%. This is significant, given that the modulus variation of the sample material may be similarly small.

The effect of indenter modulus variation with temperature will also scale with the relative modulus of the sample compared to the indenter, so for most materials with a modulus of 200 GPa or less the change in modulus of diamond will have little to no effect in the modulus measurement. For other lower modulus indenter materials, such as sapphire, the effect will be more significant.

B. Nanoindentation of fused silica

Fused silica is the standard reference material of choice for nanoindentation calibrations due to its scale-independent indentation properties of hardness and modulus due to its mechanism of deformation by densification. This allows direct calibration of indenter shape by measuring the contact stiffness at various indentation depths and relating the stiffness, using the known elastic properties, to the projected cross-sectional areas using the Oliver and Pharr method.[46]

For elevated temperature measurements, this is still a useful trait. However, the extremely low thermal conductivity of fused silica makes accurate determination of the contact temperature using the indenter as a temperature probe extremely difficult (Figure 9). This low conductivity also creates a large gradient across thicker samples from the sample heater to the sample surface creating uncertainty about the surface temperature during previous measurements.[5,14,15,20] Furthermore, this material represents a "best case scenario" for thermal drift measurements at elevated temperature, since its low thermal conductivity proportionally decreases the heat flow, and hence the thermal drift, even in the presence of relatively large thermal gradients. To address this, a thin (250 μm) piece of fused silica was acquired from Goodfellow Cambridge Ltd., UK to minimize the gradient between the sample heater and the sample surface.

However, many previous studies,[5,14] without heated indenter tips, have still shown increasing thermal drift and/or noise as a function of increasing temperature. In Figure 12(a), the load-displacement curves, which are uncorrected for thermal drift, illustrate the independence of thermal drift from the sample temperature. At all temperatures, the thermal drift is less than 0.1 nm/s. Some variation can be observed in the maximum loads and hold period load, and this is due to the load cell drift described earlier affecting on the pseudo load control set points. In all cases, the load drift is below 1 μN/s and can be corrected for in a linear manner. This is the first systematic demonstration of stable indentation at these temperatures on a reference material either in vacuum or *in situ* in an electron microscope.

Indentation results from these tests are in good agreement with previous measurements—Figure 12(b). Elastic modulus measurements agree closely with other

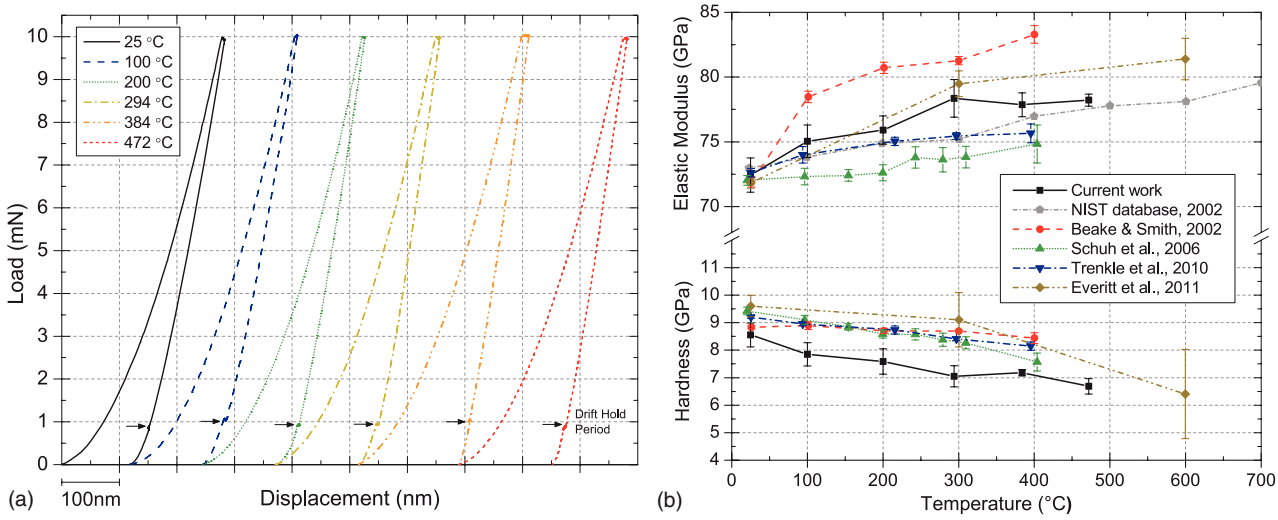

FIG. 12. Results of Berkovich indentation showing (a) load-displacement curves from each temperature uncorrected for thermal drift and offset for viewing and (b) comparison of Hardness and Elastic Modulus to literature values.[5,14,15,20,47]

measurements[15,47] taken at stable isotherms. The lower hardness values and larger standard deviations relative to the results from Trenkle *et al.*[14] or Beake and Smith[20] are attributed to a presumably higher roughness on the as-received, thin sheet of fused silica. Similar trends with temperature are observed in both hardness and elastic modulus to all observers. Some variation may also be attributed to differences between the grades of fused silica used by different investigators.

C. Micro-compression of silicon pillars

Since the first demonstration of the technique by Uchic *et al.*,[48] micro-compression has been the favored technique for *in situ* testing. This is for two reasons: the pillar shape yields a nearly uniaxial stress state for relatively straightforward stress-strain analysis and furthermore the pillar shape allows direct observation of the entire strained volume.

Currently, no standard reference material has been established for micro-compression testing in the way the fused silica has been established for nanoindentation. However, pure silicon is a low cost, accessible material which has been heavily characterized due to its status as the premier MEMS material. Silicon has good thermal conductivity, $k \approx 140$ W m^{-1} K^{-1}, which is two orders of magnitude higher than fused silica, and this allows for accurate surface temperature alignment. Like fused silica, the yield stress of silicon at lower temperatures under normal conditions is not well defined. This is due to their failure by fracture in the absence of confining pressure. However, again like fused silica, the Young's modulus of silicon is known[49,50] with good accuracy as a function of both temperature and crystallography. Unlike indentation, the confining pressure from which causes silicon to undergo a phase transformation during deformation,[51] micro-compression can be utilized to characterize the elastic anisotropy of different orientations of silicon.[52] Thus, measurements of the Young's modulus of silicon as a function of temperature from micro-compression might also be used to validate system performance.

Each sample geometry in mechanical testing requires its own analysis for accurate extraction of properties. Even conventional compression testing of macro-scale samples requires a small correction for load frame compliance or the use of a strain gauge or an extensometer. Micro-compression also requires this correction, and, for pillars which rest on a similar substrate material, a sink-in compliance must also be applied. This corrects for the effect of the pillar acting as a flat punch and elastically deforming the substrate during compression. This has been addressed using the Sneddon solution[53] by other investigators.[52,54] Assuming the pillar and the substrate have the same properties, the ratio of sink-in displacement to the total displacement can be shown to be

$$\frac{D_{Sink-In}}{D_{Total}} = \left(1 + \frac{2}{\pi(1-\nu^2)}\left(\frac{h}{a_c}\right)\right)^{-1}, \tag{2}$$

where D is displacement, ν is the Poisson's ratio, h is the pillar height, and a_c is the radius of the contact. In the case of the pillar having a fillet or radius at the base of the pillar, $a_c = r_{pillar} + r_{fillet}$, this fillet radius is added to the contact radius, enlarging the effective flat punch area.[54] This correction accounts for the elastic compliance of the bottom side of the pillar. In order to account for the elastic deformation of the flat punch indenter on the top side of the pillar, the reduced modulus concept from indentation analysis[46] is used,

$$E^* = \left(\frac{1-\nu_i^2}{E_i} + \frac{1-\nu_s^2}{E_s}\right)^{-1}, \tag{3}$$

where E^* is the reduced modulus, E_i is the indenter modulus, and E_s is the sample or pillar modulus. Finally, for elevated temperature testing, a drift hold period is used on unloading to 1/10th maximum load to measure any thermal displacement drift. This is generally corrected for with a linear fit of displacement to time.

Finally, the main limiting factor on the precision of micro-compression tests is generally the precision to which the pillar geometry is machined and measured.[30] Pillar taper causes exaggeration of work hardening parameters, since yielding occurring at the same stress will happen at increasing loads as the diameter increases. Thus, the true yield point must be calculated from the smallest cross-sectional area or narrowest diameter on the pillar. However, during elastic loading the geometry remains largely unchanged, neglecting Poisson expansion, so the elastic stress is evenly distributed. Thus, the correct diameter for measurement of elastic properties is the average diameter over the entire pillar's height, rather than the narrowest point where yielding occurs. This is why the stiffness shown in Figure 14 is higher than that shown in Figure 13.

A summary of all these corrections is shown in Figure 13(a) for data acquired at 200 °C on ⟨100⟩ silicon pillars made by lithography.[55] The room temperature micro-compression behavior of these pillars was previously described by Moser *et al.*[56] The Young's modulus as a function of temperature up to 500 °C measured by this method is shown in Figure 13(b). The precision of this method is observed to be on the order of 5%, which is in agreement with other observers.[52] Despite the encouraging accuracy of the results shown, this precision is generally insufficient to characterize a variation as small as the Young's modulus of silicon, which varies less than 1% per 100 °C. Other test geometries which incorporate significantly larger elastic deformations, such as the deformation of long micro-cantilevers or indentation using large spheres, are suggested for greater accuracy in determination of the variation of elastic properties with temperature.

The primary reason for employing the micro-pillar geometry is not to study elasticity but to study plasticity in small volumes. By performing micro-compression tests *in situ*, both stress-strain behavior and observations of deformation and failure mechanisms can be acquired simultaneously. This highlights the unique capability of the combination of high temperature and *in situ* testing to visualize transitions in behavior with temperature. Figure 14 illustrates the transitions in both stress-strain behavior and failure mechanisms of silicon with increasing temperature. At temperatures below 200 °C, pillars were observed to fail by fracture at

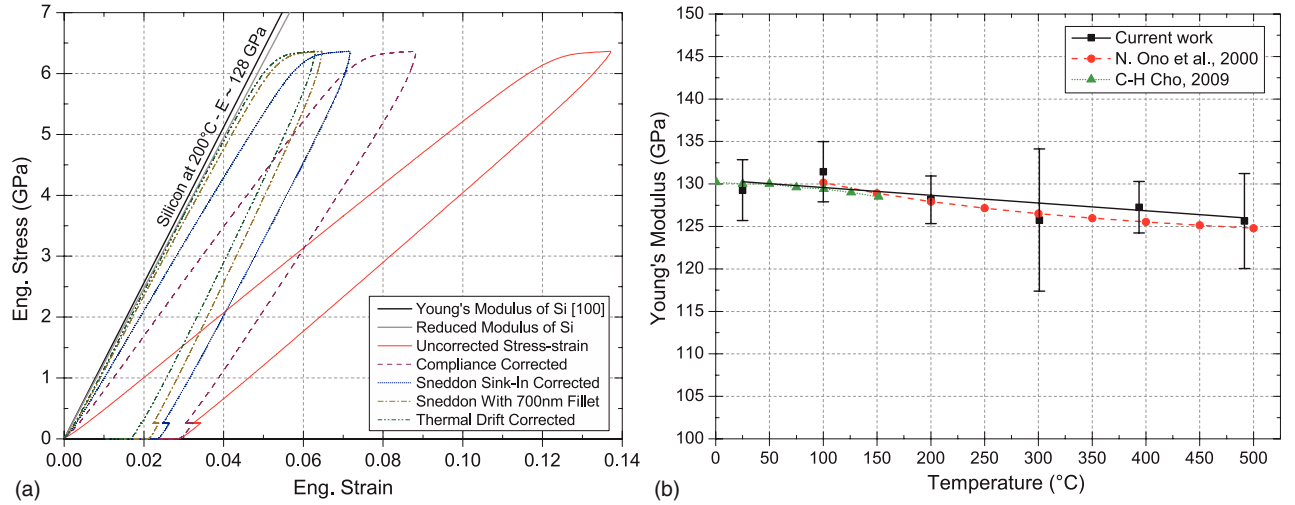

FIG. 13. Young's modulus of ⟨100⟩ silicon showing (a) corrections to micro-compression data and (b) micro-compression results compared to flexural literature values[49,50] as a function of temperature.

the base. Presumably this is due to crack nucleation from the geometric defects at the base of the pillar from etching visible in the micrographs.

At temperatures between 200 and 300 °C, pillars were observed to form splitting cracks in the bases of the pillars. This is suggested to occur by the same splitting mechanism described previously,[57–59] where two slip planes intersect to nucleate a vertical crack. Here, the crack is observed to form at the bottom of the pillars, rather than at the top as observed previously, due to these pillars being tapered towards the bottom due to etching techniques, rather than tapering towards the top due to top-down FIB milling techniques.

At temperatures greater than ∼350 °C, deformation was observed to primarily occur by slip with vertical cracking observed only rarely. At the highest temperature, 492 °C, no cracks were observed. This transition was also marked by the "classic" shape of the stress-strain curves with the appearance of a lower yield plateau consistent with "easy glide"[60] after dislocation nucleation during the upper yield point. This is the first such observation of upper and lower yield points during micro-compression testing of semiconductors, and this highlights the intrinsic displacement-controlled nature of the system. In a load-controlled system, the deformation would proceed rapidly after the upper yield point was reached, as has been observed previously during elevated temperature micro-compression of silicon by Korte *et al.*[29] In load control, careful multiple load-unload cycles would be required to see the lower yield point.

Despite the lack of a significant consensus in the literature on the precise yield stress of silicon as a function of temperature due to the difficulty of the measurement, several previous investigators[29,60–64] have acquired data suitable for comparison (Figure 15). The most closely related dataset to the current work is that of Korte *et al.*,[29] who compressed 2 μm diameter silicon pillars made by focused ion beam machining using a custom, high temperature, vacuum nanoindentation system.[18] These 2 μm pillars might be expected to be ∼15% stronger than those in the current work due to the size effect[56] in this material. However, the effect of damage from the FIB[65] producing a near-surface amorphous silicon

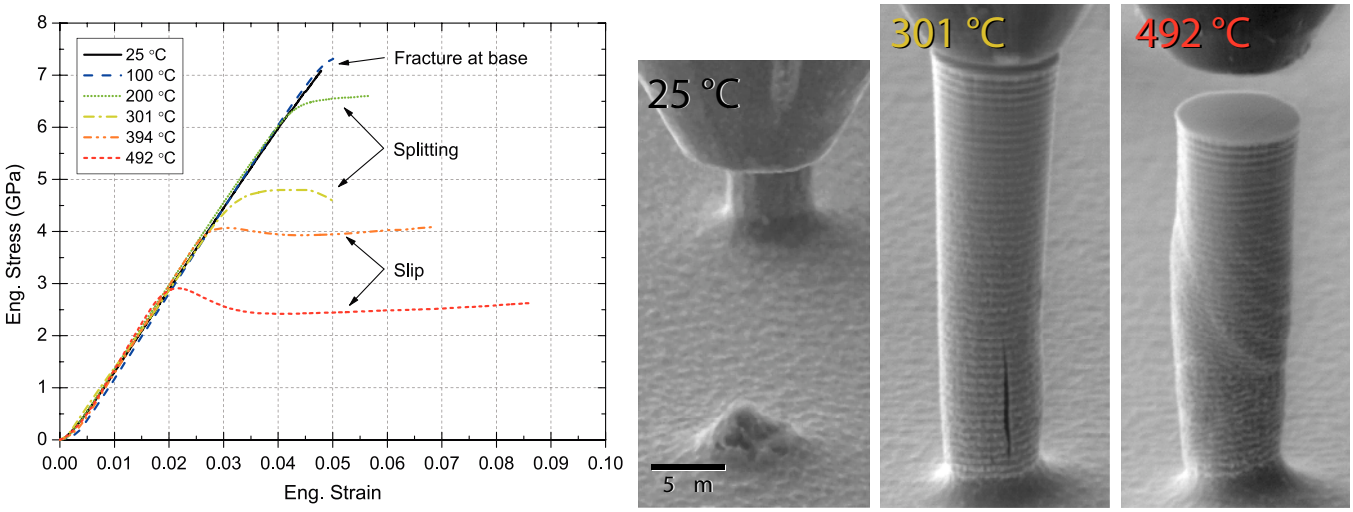

FIG. 14. Engineering stress-strain curves for ⟨100⟩ silicon as a function of temperature and accompanying *in situ* SE micrographs illustrating the failure modes.

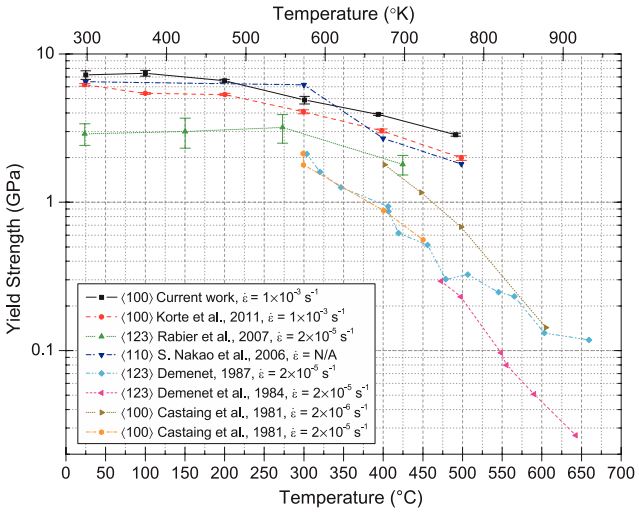

FIG. 15. Yield strength of silicon as a function of temperature comparing to literature values of upper yield from micro-compression[29] and micro-tension[61] and of lower yield values from bulk compression using high hydrostatic confining pressure.[60,62–64]

region might have lowered the dislocation nucleation stress, resulting in the ∼20% lower yield stress. The remaining difference between the micro-compression results and bulk compression results is attributed to the two orders of magnitude difference in strain rate. Good agreement is observed between micro-compression and micro-tension results, though the strain rate applied in tension was unspecified.

Overall, very good agreement is observed between the results, especially the modulus measurements, obtained using the current system and those in the literature. The trend observed by Korte *et al.*[29] is closely paralleled by the current work, and the observed deformation also agrees well with their observations. Further discussion of the current understanding of the mechanisms of deformation in silicon can be found in the referenced literature.

VI. SUMMARY AND OUTLOOK

A novel *in situ* nano-mechanical testing system capable of stable operation at elevated temperatures in the SEM has been described. Elevated temperatures within the system are highly localized to the test region, and rapid thermal stabilization of the system is achieved using a compact design and high thermal conductivity frame components.

Contact thermal drift occurs due to heat flow at the contact, so it is proportional to magnitude and direction of heat transfer. Temperature monitoring of the indenter allows for this to be directly observed and for rapid matching of the sample and indenter temperatures during the frame stabilization period. This allows significant time savings over the displacement drift tuning approach, which requires the system be absolutely stable before displacement drift can be measured. Additionally, use of a thermally calibrated indenter allows testing to be performed with the surface temperatures known to an accuracy of ∼1%. The sensitivity of the indenter as a temperature probe has been discussed, and a novel method for local thermal conductivity measurement has been proposed. Additional procedures and considerations for elevated temperature testing have also been discussed (see Table I).

Validation of the system performance at elevated temperature was achieved by using two methods to measure the Young's modulus of known reference materials. High temperature Berkovich nanoindentation on fused silica demonstrated the low thermal drifts achievable at temperatures up to ∼500 °C with good measurement accuracy even at low indentation depths. Furthermore, micro-compression measurements of the Young's modulus of ⟨100⟩ silicon pillars demonstrated the system's thermal stability on materials of high thermal conductivity, as well. Micro-compression stress-strain measurements also highlight the advantages of the intrinsic displacement control of the system, which allows it to function as a micro-scale load frame. These include true strain rate control which yielded the classic upper and lower yield point phenomenon in silicon deformation at high temperatures. The utility of the combination of *in situ* observation and elevated temperature is clearly demonstrated by the observed transitions in deformation mechanism of silicon with increasing temperature.

With a general understanding of the behavior of nano-mechanical testing systems at elevated temperatures achieved, the outlook for system development is very promising. Current temperature and sensor precision limitations all have existing technological solutions, so extension of this system or similar systems to higher temperatures with improved load and displacement resolution is expected. Extensive

TABLE I. Summary of various high temperature challenges and solutions presented in this work.

High temperature challenge	Solution
Frame compliance variation with temperature	Watercool frame to prevent changes in frame modulus and/or use high temperature materials with negligible modulus change within temperature range
Sensor/actuator calibrations change with temperature	Remove sensors/actuators from hot zone using insulators and active cooling
Contact surface temperature uncertainty	Measure surface temperature directly with surface mounted thermocouple or thermally instrumented and calibrated indenter, then match indenter temperature to sample surface temperature
Excessive thermal drift during testing	Increase stabilization time or tune indenter/sample temperatures for closer match
Indenter reacts with environment/sample	Exchange indenter material for more chemically stable material, e.g., use sapphire instead of diamond for indenting steels or in oxygen
Sample/indenter oxidizes at temperature	Implement system inside a vacuum chamber or environmental chamber with inert gas

application of this technology to research of a wide variety of materials due to the general utility of temperature and strain rate variability is anticipated.

ACKNOWLEDGMENTS

The authors would like to thank S. Fahlbusch of Alemnis and D. Frey and G. Buerki of EMPA for technical assistance with the *In Situ* Indenter and S. Hostettler of Synton-MDP AG, Nidau, Switzerland for help with the joint development of the heated indenter tips used in this work. The authors would also like to thank O. Torrents Abad and A. Schneider of the Leibniz-Institut für Neue Materialien, Saarbrücken, Germany for preparation of the tantalum sample.

[1]D. S. Gianola and C. Eberl, JOM **61**(3), 24–35 (2009).
[2]D. Kiener, C. Motz, G. Dehm, and R. Pippan, Int. J. Mater. Res. **100**(8), 1074–1087 (2009).
[3]M. Legros, D. S. Gianola, and C. Motz, MRS Bull. **35**(5), 354–360 (2010).
[4]S. Syed Asif, K. Wahl, R. Colton, and O. Warren, J. Appl. Phys. **90**(3), 1192–1200 (2001).
[5]C. A. Schuh, C. E. Packard, and A. C. Lund, J. Mater. Res. **21**(3), 725–736 (2006).
[6]C. Niederberger, W. M. Mook, X. Maeder, and J. Michler, Mater. Sci. Eng., A **527**(16–17), 4306–4311 (2010).
[7]X. Maeder, W. M. Mook, C. Niederberger, and J. Michler, Philos. Mag. **91**(7–9), 1097–1107 (2011).
[8]R. Ghisleni, J. Liu, R. Raghavan, P. Brodard, A. Lugstein, K. Wasmer, and J. Michler, Philos. Mag. **91**(7–9), 1286–1292 (2010).
[9]S. Ruffell, J. Bradby, J. Williams, and O. Warren, J. Mater. Res. **22**(03), 578–586 (2007).
[10]L. Fang, C. L. Muhlstein, J. G. Collins, A. L. Romasco, and L. H. Friedman, J. Mater. Res. **23**(09), 2480–2485 (2008).
[11]H. H. Nguyen, P. J. Wei, and J. F. Lin, Adv. Nat. Sci.: Nanosci. Nanotechnol. **2**(1), 015007 (2011).
[12]M. Smolka, C. Motz, T. Detzel, W. Robl, T. Griesser, A. Wimmer, and G. Dehm, Rev. Sci. Instrum. **83**(6), 064702 (2012).
[13]Z. Duan and A. Hodge, JOM **61**(12), 32–36 (2009).
[14]J. C. Trenkle, C. E. Packard, and C. A. Schuh, Rev. Sci. Instrum. **81**(7), 073901 (2010).
[15]N. M. Everitt, M. I. Davies, and J. F. Smith, Philos. Mag. **91**(7–9), 1221–1244 (2011).
[16]K. V. Rajulapati, M. M. Biener, J. Biener, and A. M. Hodge, Philos. Mag. Lett. **90**(1), 35–42 (2009).
[17]J. M. Wheeler, R. Raghavan, and J. Michler, Mater. Sci. Eng., A **528**(29–30), 8750–8756 (2011).
[18]S. Korte, R. J. Stearn, J. M. Wheeler, and W. J. Clegg, J. Mater. Res. **27**(1), 167–176 (2011).
[19]J. F. Smith and S. Zheng, Surf. Eng. **16**(2), 143–146 (2000).
[20]B. D. Beake and J. F. Smith, Philos. Mag. A **82**(10 SPEC.), 2179–2186 (2002).
[21]B. Beake, S. Goodes, and J. Smith, Z. Metallkd. **94**(7), 1–7 (2003).
[22]J. Xia, C. X. Li, and H. Dong, Mater. Sci. Eng., A **354**, 112–120 (2003).
[23]G. Fox-Rabinovich, B. Beake, J. Endrino, S. Veldhuis, R. Parkinson, L. Shuster, and M. Migranov, Surf. Coat. Technol. **200**, 5738–5742 (2006).
[24]B. Beake, J. Smith, A. Gray, G. Fox-Rabinovich, S. Veldhuis, and J. Endrino, Surf. Coat. Technol. **201**, 4585–4593 (2007).
[25]A. Gray and B. D. Beake, J. Nanosci. Nanotechnol. **7**(7), 2530–2533 (2007).
[26]A. J. Muir Wood and T. W. Clyne, Acta Mater. **54**(20), 5607–5615 (2006).
[27]A. J. Muir Wood, S. Sanjabi, Y. Q. Fu, Z. H. Barber, and T. W. Clyne, Surf. Coat. Technol. **202**, 3115–3120 (2008).
[28]S. Korte and W. J. Clegg, Scr. Mater. **60**(9), 807–810 (2009).
[29]S. Korte, J. S. Barnard, R. J. Stearn, and W. J. Clegg, Int. J. Plast. **27**(11), 1853–1866 (2011).
[30]J. M. Wheeler, C. Niederberger, C. Tessarek, S. Christiansen, and J. Michler, Int. J. Plast. **40**, 140–151 (2013).
[31]J. M. Wheeler, R. Raghavan, and J. Michler, Scr. Mater. **67**(0), 125–128 (2012).
[32]J. M. Wheeler, P. Brodard, and J. Michler, Philos. Mag. **92**(25–27), 3128–3141 (2012).
[33]J. Pfetzing-Micklich, R. Ghisleni, T. Simon, C. Somsen, J. Michler, and G. Eggeler, Mater. Sci. Eng., A **538**, 265–271 (2012).
[34]J. M. Wheeler, R. A. Oliver, and T. W. Clyne, Diamond Relat. Mater. **19**(11), 1348–1353 (2010).
[35]R. Rabe, J. M. Breguet, P. Schwaller, S. Stauss, F. J. Haug, J. Patscheider, and J. Michler, Thin Solid Films **469–470**, 206–213 (2004).
[36]R. Ghisleni, K. Rzepiejewska-Malyska, L. Philippe, P. Schwaller, and J. Michler, Microsc. Res. Tech. **72**(3), 242–249 (2009).
[37]J. W. Draper, London, Edinburgh Dublin Philos. Mag. J. Sci. **30**, 345–359 (1847).
[38]F. Giuliani, Ph.D. dissertation, University of Cambridge, 2005.
[39]J. Holman, *Heat Transfer*, 7th ed. (McGraw-Hill, London, 1992).
[40]CRC, *Handbook of Chemistry and Physics*, 57th ed. (CRC Press, Cleveland, 1976).
[41]F. Aguado and V. G. Baonza, Phys. Rev. B **73**(2), 024111 (2006).
[42]S. R. Murthy, J. Mater. Sci. Lett. **4**(5), 603–605 (1985).
[43]Z. Li and R. C. Bradt, Int. J. High Technol. Ceram. **4**(1), 1–10 (1988).
[44]T. Goto, O. L. Anderson, I. Ohno, and S. Yamamoto, J. Geophys. Res. **94**(B6), 7588–7602, doi:10.1029/JB094iB06p07588 (1989).
[45]J. B. Wachtman, Jr., W. E. Tefft, D. G. Lam, Jr., and C. S. Apstein, Phys. Rev. **122**(6), 1754–1759 (1961).
[46]W. C. Oliver and G. M. Pharr, J. Mater. Res. **7**(6), 1564–1583 (1992).
[47]R. G. Munro, *NISTIR 6853* (NIST, Gaithersburg, MD, 2002).
[48]M. D. Uchic, D. M. Dimiduk, J. N. Florando, and W. D. Nix, Science **305**(5686), 986–989 (2004).
[49]N. Ono, K. Kitamura, K. Nakajima, and Y. Shimanuki, Jpn. J. Appl. Phys. **39**, 368–371 (2000).
[50]C.-H. Cho, Curr. Appl. Phys. **9**(2), 538–545 (2009).
[51]L. J. Vandeperre, F. Giuliani, S. J. Lloyd, and W. J. Clegg, Acta Mater. **55**(18), 6307–6315 (2007).
[52]I.-S. Choi, Y. Gan, D. Kaufmann, O. Kraft, and R. Schwaiger, J. Mater. Res. **27**, 2752–2759 (2012).
[53]I. N. Sneddon, Proc. Cambridge Philos. Soc. **42**, 29–39 (1946).
[54]H. Zhang, B. E. Schuster, Q. Wei, and K. T. Ramesh, Scr. Mater. **54**(2), 181–186 (2006).
[55]L. Barbieri, E. Wagner, and P. Hoffmann, Langmuir **23**(4), 1723–1734 (2007).
[56]B. Moser, K. Wasmer, L. Barbieri, and J. Michler, J. Mater. Res. **22**(4), 1004–1011 (2007).
[57]F. Östlund, K. Rzepiejewska-Malyska, K. Leifer, L. M. Hale, Y. Tang, R. Ballarini, W. W. Gerberich, and J. Michler, Adv. Funct. Mater. **19**(15), 2439–2444 (2009).
[58]F. Ostlund, P. Howie, R. Ghisleni, S. Korte, K. Leifer, W. Clegg, and J. Michler, Philos. Mag. **91**(7–9), 1190–1199 (2011).
[59]P. R. Howie, S. Korte, and W. J. Clegg, J. Mater. Res. **27**(01), 141–151 (2012).
[60]J. Rabier, P. O. Renault, D. Eyidi, J. L. Demenet, J. Chen, H. Couvy, and L. Wang, Phys. Status Solidi C **4**(8), 3110–3114 (2007).
[61]S. Nakao, T. Ando, M. Shikida, and K. Sato, J. Micromech. Microeng. **16**(4), 715–720 (2006).
[62]J. Castaing, P. Veyssiere, L. P. Kubin, and J. Rabier, Philos. Mag. A **44**(6), 1407–1413 (1981).
[63]J. L. Demenet, Ph.D. dissertation, University of Poitiers, France, 1987.
[64]J. L. Demenet, J. C. Desoyer, J. Rabier, and P. Veyssiere, Scr. Metall. **18**(1), 41–45 (1984).
[65]S. Shim, H. Bei, M. K. Miller, G. M. Pharr, and E. P. George, Acta Mater. **57**(2), 503–510 (2009).